



Thermo-elastic-viscoplastic-damage model for self-heating and mechanical behavior of thermoplastic polymers

Fei Shen^a, Guozheng Kang^b, Yee Cheong Lam^a, Yujie Liu^b, Kun Zhou^{a,c,*}

^a School of Mechanical and Aerospace Engineering, Nanyang Technological University, 50 Nanyang Avenue, Singapore, 639798, Singapore

^b School of Mechanics and Engineering, Southwest Jiaotong University, Chengdu, 610031, China

^c Environment Process Modelling Centre, Nanyang Environment & Water Research Institute, Nanyang Technological University, 1 Cleantech Loop, Singapore, 637141, Singapore

ARTICLE INFO

Keywords:

Constitutive modeling
Self-heating
Viscoplastic
Damage
Thermoplastic polymer

ABSTRACT

A thermo-elastic-viscoplastic-damage model based on thermodynamics is developed to describe the self-heating and stress-strain behavior of thermoplastic polymers under tensile loading. The constitutive model considers temperature-dependent elasticity, nonlinear viscoplastic flow and damage evolution. The model includes the important self-heating of a polymer caused by the viscoplasticity and the often neglected damage energy dissipation during deformation. The model parameters are calibrated from the monotonic and repeated loading tests for polyamide 6 under different temperatures and loading rates. In particular, the damage evolution is evaluated by the stiffness reduction in the repeated loading tests. The proposed model is implemented in a finite element package to predict the self-heating and mechanical behavior of the polymer at a high loading rate. The predicted temperature and load evolution curves agree with the experimental data.

1. Introduction

Thermoplastic polymers have been widely used to fabricate engineering components in industrial sectors ranging from automotive, aerospace to biomedical fields due to their excellent impact resistance, high strength-to-weight ratio and good bio-affinity (Ramakrishna et al., 2001). A good understanding of their mechanical behavior and intrinsic deformation mechanisms is of prime significance for the design, manufacturing and reliability assessment of the components.

The mechanical behavior of thermoplastic polymers has been extensively investigated in the past half-century (Barentsen and Heikens, 1973; Bax and Müssig, 2008; Kennedy et al., 1994; Mullins, 1948; Nielsen, 1969). Thermoplastic polymers consist of long and flexible chains interlinked through hydrogen and van der Waals bonds. Either the chains are all randomly oriented to form amorphous polymers, or some portions of them fold together in an orderly arrangement to form crystalline phases in semi-crystalline polymers. Under tensile loading, amorphous chains are stretched and gradually aligned with the loading direction. The crystalline regions are torn apart due to the slide of the arranged chains, and finally transformed into a highly oriented fibrillar structure at large strain (Jabbari-Farouji et al., 2015). Through macroscopic experimental observations, thermoplastic polymers typically exhibit elastic or viscoelastic behavior at small deformation and visco-elastic-plastic behavior at large deformation. Furthermore, damage occurs due to irreversible changes in the microstructures during deformation (e.g., the initiation, enlargement and coalescence of micro-voids (Zaïri et al., 2011) or plastic deformation in the crystalline regions (Detrez et al., 2011)). It causes polymers to experience

* Corresponding author.

E-mail address: kzhou@ntu.edu.sg (K. Zhou).

<https://doi.org/10.1016/j.ijplas.2019.06.003>

Received 31 January 2019; Received in revised form 16 May 2019; Accepted 7 June 2019

Available online 13 June 2019

0749-6419/ © 2019 Elsevier Ltd. All rights reserved.

specific mechanical behavior such as strain softening for amorphous polymers under monotonic loading (Nguyen et al., 2016), Mullins effect for styrene-butadiene rubber under cyclic loading (Ayoub et al., 2011b) and stiffness reduction under repeated loading tests (Balieu et al., 2013). Besides, localized damage and plastic deformation lead to the onset of necking at high strain before the breaking of polymers.

Loading conditions, especially temperature and strain rate, affect the mechanical response of thermoplastic polymers (Boyce et al., 1994; Chen et al., 2002, 2016; Hine et al., 2005). Temperature has a significant effect on the elastic modulus and yield stress of thermoplastic polymers. The mobility of amorphous chains increases significantly with an increase in temperature, especially in the rubber-glass transition region. It leads to a significant decrease of the elastic modulus and yield stress as the polymers change from the glassy state to the rubbery state. Moreover, volume increases in an increasing rate. For some amorphous polymers such as polycarbonate and polymethylmethacrylate, the stress-strain responses in the glassy and the rubbery states have obvious differences (Srivastava et al., 2010). Conversely, material temperature is influenced by its deformation. The energy dissipation due to the viscoplastic flow causes self-heating of thermoplastic polymers (Maurel-Pantel et al., 2015; Ovalle Rodas et al., 2014). The strain rate influences the yielding and viscoplastic flow behavior of thermoplastic polymers. The increase of strain rate leads to continuous hardening after yielding. Meanwhile, the self-heating phenomenon is also influenced by the strain rate (Maurel-Pantel et al., 2015). Higher strain rate leads to larger increment of the temperature. Therefore, there is competition between softening (caused by self-heating and damage) and hardening (induced by strain rate) during deformation.

Thermo-mechanical constitutive models have been proposed to interpret the mechanical behavior of thermoplastic polymers with time and temperature dependencies. Arruda et al. (1995) modified an elastic-viscoplastic model (Boyce et al., 1988) originally for isothermal conditions to reproduce the temperature-dependent mechanical behavior of polymethylmethacrylate. The shear modulus was defined as a logarithmic function of temperature. Srivastava et al. (2010) developed a thermo-mechanical model to study the elastic-viscoplastic behavior of three thermoplastic polymers over a wide temperature range spanning their glass transition temperatures. In addition, the effect of rubber-glass transition on the thermo-mechanical behavior has been considered in the modeling of several amorphous polymers (Anand et al., 2009; Buckley and Jones, 1995; Dooling et al., 2002; Dupaux and Boyce, 2007; Mathiesen et al., 2014; Xiao et al., 2017). Bouvard et al. (2013) used three microstructure-based internal state variables in a thermo-mechanical model to describe the micro-mechanisms of chain deformation. Inspired by the model developed for isothermal condition (Polanco-Loria et al., 2010), Garcia-Gonzalez et al. (2017) developed a thermo-hyperelastic-viscoplastic model with consideration of strain rate-dependent material hardening, self-heating caused by plastic dissipation, and material expansion. Yu et al. (2017b) proposed a thermo-mechanical model to evaluate the cyclic viscoelastic-viscoplastic response of polyethylene with ultra-high molecular weight. More recently, Yu et al. (2017a) extended their previous model to consider the effect of chemical reaction and moisture diffusion on the cyclic mechanical behavior of polyamide 6. The multi-physical coupling relationship was considered in the proposed hydro-thermo-viscoelastic-viscoplastic model.

Damage behavior can be included in the constitutive modeling for the mechanical behavior of thermoplastic polymers. These constitutive models generally can be categorized into two classes: micromechanics and continuum damage mechanics (CDM) methods.

The micromechanics method considers the damage process as the growth of voids as well as their interactions within the material. The Gurson model and its modified versions (Gurson, 1977; Nahshon and Hutchinson, 2008; Tvergaard, 1982), originally for porous metallic materials, were extended to investigate void growth in thermoplastic polymers. The hydrostatic pressure dependency (Jeong and Pan, 1995; Lazzeri and Bucknall, 1995) and the strain rate sensitivity (Challier et al., 2006; Zairi et al., 2005) were considered in the modeling. Zairi et al. (2011) further considered voids growth with anisotropic behavior in rubber-toughened polymers at large deformation. The advantage of a micromechanics method is that it provides a connection between microstructures (voids, cracks and matrix) and mechanical behavior of polymers. However, the resulting models are complicated with material parameters regarding the distribution and evolution of microstructures, which are difficult to calibrate from the overall mechanical behavior.

The CDM method, in contrast, introduces a damage variable (scalar or tensor) to represent the material degradation at the macroscopic scale induced by micro-voids and micro-cracks (Al-Rub and Voyiadjis, 2003; Haddag et al., 2009; Lemaitre and Chaboche, 1994; Shen et al., 2015, 2017; Voyiadjis and Dorgan, 2007). The coupling relationships between stress, elastic strain, plastic strain and damage can be considered intrinsically in the thermodynamic framework. Ayoub et al. (2011a) and Ayoub et al. (2011b) proposed visco-hyperelastic-damage models for high-cycle and low-cycle fatigue behavior of styrene-butadiene rubber, respectively. The deterioration of mechanical behavior during cyclic loading was explained through the network alteration theory in which a damage variable was introduced to represent the change in the number of chain segments. Balieu et al. (2013) developed an elastic-viscoplastic-damage model for 20% mineral-filled polypropylene with consideration of the non-isochoric deformation and the hydrostatic pressure dependency. Two methods to calculate the evolution of damage during deformation were proposed, one using the reduction of stiffness and the other using the variation of stresses under compressible and incompressible assumptions. Comparing with the micromechanics method, damage variable and its evolution in the CDM method can be identified from the macroscopic mechanical behavior of thermoplastic polymers.

It should be highlighted that hitherto the CDM-based models for the mechanical response of thermoplastic polymers are limited to isothermal conditions. Indeed, the damage should be appropriately incorporated in a thermo-mechanical model for a better description of the mechanical response. The effect of damage on self-heating, although important, is yet to be considered in the constitutive modeling. Furthermore, the influence of temperature on the damage evolution of polymers has never been studied.

Therefore, this study presents a thermo-elastic-viscoplastic-damage model to address the above shortcomings. The model aims to describe the thermo-mechanical response of thermoplastic polymers during finite deformation, taking into consideration of damage and self-heating. Based on thermodynamics, the coupling relationship between damage and elasticity as well as viscoplasticity is

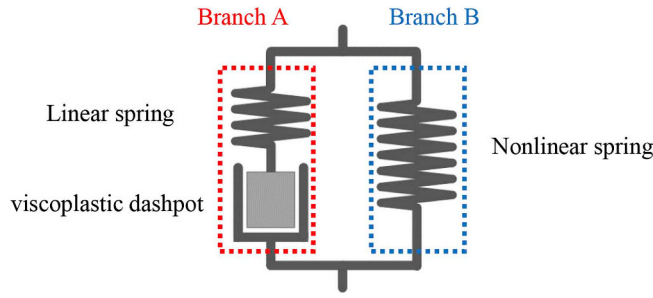


Fig. 1. Schematic of the constitutive model with three elements.

considered in the model by including damage in the specific Helmholtz free energy and the viscoplastic dissipation potential. Moreover, the energy dissipations from both damage and viscoplastic deformation are considered as the heat source in the model for causing self-heating. The mechanical behavior and the temperature evolution of a semi-crystalline polyamide 6 are experimentally investigated under different temperatures and loading rates. In particular, the damage evolution during deformation is evaluated through repeated loading tests at different temperatures. The model parameters are calibrated from the results of the monotonic and repeated loading tests. The self-heating tests are conducted to study the mechanical behavior and temperature evolution at a high loading rate. In conjunction with the finite element method, the proposed model is employed to reproduce the temperature evolution and mechanical behavior in the self-heating tests. The predicted results of the temperature increment and load evolution are compared with the experimental data.

2. Constitutive model

The mechanical behavior of thermoplastic polymers is schematically represented by the deformation of two parallel branches as shown in Fig. 1 (Boyce et al., 2000; Holopainen et al., 2017; Ovalle Rodas et al., 2014; Torres et al., 2016). Branch A, consisting of a linear elastic spring and a viscoplastic dashpot, represents the elastic response at small deformation and the viscoplastic flow with temperature and strain rate dependencies at moderate deformation. The nonlinear spring in branch B is used to describe the strain hardening behavior at large deformation. The kinematics and thermodynamics will be revisited to formulate the associated constitutive model of thermoplastic polymers.

2.1. Kinematics

Three configurations shown in Fig. 2 are established to describe the kinematics of finite deformation in thermoplastic polymers. As two elements are used in branch A, a relaxed configuration $\bar{\Omega}$ is proposed between the reference and current configurations to distinguish the deformation of each element (i.e., the elastic and viscoplastic deformation). With a parallel design, the deformation gradients of the two branches, F_A and F_B , are identical to the overall deformation gradient F :

$$F_A = F_B = F. \tag{1}$$

According to the two elements in branch A, the deformation gradient is divided into an elastic component F_A^e and a viscoplastic component F_A^p :

$$F_A = F_A^e F_A^p. \tag{2}$$

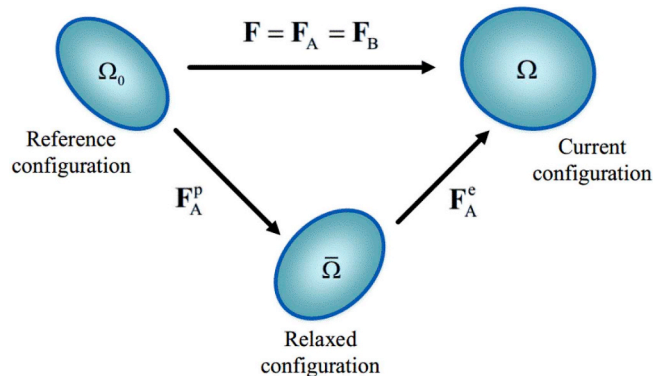


Fig. 2. Schematic representation of deformation gradients in three configurations.

The velocity gradient \mathbf{L}_A of branch A is written as

$$\mathbf{L}_A = \dot{\mathbf{F}}_A \mathbf{F}_A^{-1} = \mathbf{L}_A^e + \mathbf{F}_A^e \bar{\mathbf{L}}_A^p (\mathbf{F}_A^e)^{-1}, \tag{3}$$

where $\mathbf{L}_A^e = \dot{\mathbf{F}}_A^e (\mathbf{F}_A^e)^{-1}$ and $\bar{\mathbf{L}}_A^p = \dot{\mathbf{F}}_A^p (\mathbf{F}_A^p)^{-1}$ are the elastic part and the viscoplastic part, respectively. The elastic part can further be divided into symmetric and skew components, i.e., $\mathbf{L}_A^e = \mathbf{D}_A^e + \mathbf{W}_A^e$, the elastic rate-of-deformation tensor is given as $\mathbf{D}_A^e = (\dot{\mathbf{F}}_A^e (\mathbf{F}_A^e)^{-1} + (\mathbf{F}_A^e)^{-T} (\dot{\mathbf{F}}_A^e)^T) / 2$. It is noted that the viscoplastic part $\bar{\mathbf{L}}_A^p$ is expressed in the relaxed configuration.

The velocity gradient of branch B can be written as

$$\mathbf{L}_B = \dot{\mathbf{F}}_B \mathbf{F}_B^{-1} = \mathbf{D}_B + \mathbf{W}_B, \tag{4}$$

where \mathbf{D}_B and \mathbf{W}_B are the symmetric and skew components of \mathbf{L}_B , respectively.

The total stress is the combination of the contributions from these two branches:

$$\boldsymbol{\sigma} = \boldsymbol{\sigma}_A + \boldsymbol{\sigma}_B. \tag{5}$$

2.2. Thermodynamics

Thermodynamics is used to formulate the relationships between stress, strain, damage, temperature and loading rate. The first thermodynamic principle is expressed in the current configuration as (Belytschko et al., 2013; Lemaitre and Chaboche, 1994)

$$\rho \dot{w} = \boldsymbol{\sigma} : \mathbf{D} - \nabla \cdot \mathbf{q} + \rho \phi, \tag{6}$$

where the Cauchy stress $\boldsymbol{\sigma}$ includes the contributions from the two branches, the term $\boldsymbol{\sigma} : \mathbf{D}$ is the rate of strain energy density, the vector \mathbf{q} represents the heat flux, the three scalars ρ , w and ϕ represent the density, internal energy and external heat source, respectively. By using Eqs. (3) and (4), Eq. (6) is written as

$$\rho \dot{w} = \boldsymbol{\sigma}_A : \mathbf{L}_A^e + \boldsymbol{\sigma}_A : \mathbf{F}_A^e \bar{\mathbf{L}}_A^p (\mathbf{F}_A^e)^{-1} + \boldsymbol{\sigma}_B : \mathbf{L}_B - \nabla \cdot \mathbf{q} + \rho \phi, \tag{7}$$

where the equation $\boldsymbol{\sigma} : \mathbf{D} = \boldsymbol{\sigma} : \mathbf{L}$ is used. The Clausius-Duhem inequality based on the second thermodynamic principle is written as (Lemaitre and Chaboche, 1994)

$$\rho \dot{s} + \nabla \cdot \frac{\mathbf{q}}{T} - \frac{\rho \dot{\phi}}{T} \geq 0, \tag{8}$$

where T represents the material temperature and s is the specific entropy. By using the specific Helmholtz free energy $\psi = w - sT$ and substituting the term $\rho \dot{\phi}$ using Eq. (7), the above inequality is expressed as

$$-\rho \dot{\psi} - \rho s \dot{T} - \frac{\nabla T}{T} \cdot \mathbf{q} + \boldsymbol{\sigma}_A : \mathbf{L}_A^e + \boldsymbol{\sigma}_A : \mathbf{F}_A^e \bar{\mathbf{L}}_A^p (\mathbf{F}_A^e)^{-1} + \boldsymbol{\sigma}_B : \mathbf{L}_B \geq 0. \tag{9}$$

The Helmholtz free energy is considered as a function of deformation, damage and temperature of the two branches: $\psi = \psi(\mathbf{C}_A^e, \mathbf{C}_B, D, T)$, where the scalar D is the damage variable under isotropic damage assumption, $\mathbf{C}_A^e = (\mathbf{F}_A^e)^T \mathbf{F}_A^e$ is the elastic Cauchy–Green tensor of branch A and $\mathbf{C}_B = \mathbf{F}_B^T \mathbf{F}_B$ is the Cauchy–Green tensor of branch B. The derivative of ψ is calculated as

$$\dot{\psi} = \frac{\partial \psi}{\partial \mathbf{C}_A^e} : \dot{\mathbf{C}}_A^e + \frac{\partial \psi}{\partial \mathbf{C}_B} : \dot{\mathbf{C}}_B + \frac{\partial \psi}{\partial D} \dot{D} + \frac{\partial \psi}{\partial T} \dot{T}. \tag{10}$$

The first item at the right side of Eq. (10) is expressed as

$$\frac{\partial \psi}{\partial \mathbf{C}_A^e} : \dot{\mathbf{C}}_A^e = \frac{\partial \psi}{\partial \mathbf{C}_A^e} : ((\dot{\mathbf{F}}_A^e)^T \mathbf{F}_A^e + (\mathbf{F}_A^e)^T \dot{\mathbf{F}}_A^e) = \mathbf{F}_A^e \frac{\partial \psi}{\partial \mathbf{C}_A^e} (\mathbf{F}_A^e)^T : ((\mathbf{F}_A^e)^{-T} (\dot{\mathbf{F}}_A^e)^T + \dot{\mathbf{F}}_A^e (\mathbf{F}_A^e)^{-1}) = 2 \mathbf{F}_A^e \frac{\partial \psi}{\partial \mathbf{C}_A^e} (\mathbf{F}_A^e)^T : \mathbf{D}_A^e. \tag{11}$$

Similarly, the second item is written as

$$\frac{\partial \psi}{\partial \mathbf{C}_B} : \dot{\mathbf{C}}_B = 2 \mathbf{F}_B \frac{\partial \psi}{\partial \mathbf{C}_B} \mathbf{F}_B^T : \mathbf{D}_B. \tag{12}$$

By substituting Eqs. (10)–(12) into Eq. (9), the Clausius-Duhem inequality can be written as

$$-\rho \left(s + \frac{\partial \psi}{\partial T} \right) \dot{T} + \left(\boldsymbol{\sigma}_A - 2 \mathbf{F}_A^e \rho \frac{\partial \psi}{\partial \mathbf{C}_A^e} (\mathbf{F}_A^e)^T \right) : \mathbf{D}_A^e + \left(\boldsymbol{\sigma}_B - 2 \mathbf{F}_B \rho \frac{\partial \psi}{\partial \mathbf{C}_B} \mathbf{F}_B^T \right) : \mathbf{D}_B + \boldsymbol{\sigma}_A : \mathbf{F}_A^e \bar{\mathbf{L}}_A^p (\mathbf{F}_A^e)^{-1} - \rho \frac{\partial \psi}{\partial D} \dot{D} - \frac{\nabla T}{T} \cdot \mathbf{q} \geq 0. \tag{13}$$

Since Eq. (13) should be fulfilled for any admissible deformation and temperature history, the following constitutive equations are obtained as

$$s = - \frac{\partial \psi}{\partial T}, \tag{14}$$

$$\boldsymbol{\sigma}_A = 2 \mathbf{F}_A^e \rho \frac{\partial \psi}{\partial \mathbf{C}_A^e} (\mathbf{F}_A^e)^T, \tag{15}$$

$$\sigma_B = 2F_B \rho \frac{\partial \psi}{\partial C_B} F_B^T \tag{16}$$

The damage energy release rate Y that is conjugated to D can be defined according to Eq. (13):

$$Y = -\rho \frac{\partial \psi}{\partial D} \tag{17}$$

By taking advantage of Eqs. 14–17, the Clausius-Duhem inequality is expressed as

$$\sigma_A: F_A^e \bar{L}_A^p (F_A^e)^{-1} + Y\dot{D} - \frac{\nabla T}{T} \cdot \mathbf{q} \geq 0. \tag{18}$$

The first three terms of the inequality represent the viscoplastic energy dissipation, the damage-induced energy dissipation, and the thermal dissipation, respectively. The specific Helmholtz free energy will be given in Section 2.4 to deduce the constitutive equations.

The kinetic laws governing the evolutions of the viscoplastic deformation gradient F_A^p and damage D are determined by a dissipation potential function φ . It is necessary to fulfill the inequality and thus the dissipation potential should be a convex function of the stress σ_A and the damage energy release rate Y . The evolution laws are written as

$$F_A^e \bar{L}_A^p (F_A^e)^{-1} = \dot{\lambda}_p \mathbf{N}, \tag{19}$$

$$\mathbf{N} = \sqrt{\frac{3}{2}} \frac{1}{\sqrt{\frac{\partial \varphi}{\partial \sigma_A} \cdot \frac{\partial \varphi}{\partial \sigma_A}}} \frac{\partial \varphi}{\partial \sigma_A}, \tag{20}$$

$$\dot{D} = \dot{\lambda}_D \frac{\partial \varphi}{\partial Y}, \tag{21}$$

where the tensor \mathbf{N} represents the direction of the viscoplastic flow, $\dot{\lambda}_p$ and $\dot{\lambda}_D$ are the viscoplastic and damage multipliers, respectively. The specific evolution rates will be provided in Sections 2.5 and 2.6.

2.3. Heat equation

The self-heating of thermoplastic polymers is caused by the energy dissipations from the viscoplastic deformation and the damage process. The heat equation can be derived from the first thermodynamic principle. According to Eq. (14), the time derivative of s is expressed as

$$\dot{s} = -\frac{\partial^2 \psi}{\partial T \partial C_A^e} : \dot{C}_A^e - \frac{\partial^2 \psi}{\partial T \partial C_B} : \dot{C}_B - \frac{\partial^2 \psi}{\partial T \partial D} \dot{D} - \frac{\partial^2 \psi}{\partial T^2} \dot{T}. \tag{22}$$

Using $\dot{w} = \dot{\psi} + s\dot{T} + T\dot{s}$, the time derivative of w is written as

$$\rho \dot{w} = \rho \dot{\psi} + \rho s \dot{T} - \rho T \frac{\partial^2 \psi}{\partial T \partial C_A^e} : \dot{C}_A^e - \rho T \frac{\partial^2 \psi}{\partial T \partial C_B} : \dot{C}_B - \rho T \frac{\partial^2 \psi}{\partial T \partial D} \dot{D} - \rho T \frac{\partial^2 \psi}{\partial T^2} \dot{T}. \tag{23}$$

The term $\rho \dot{w}$ and $\rho \dot{\psi}$ can be substituted using Eqs. (7) and (10), respectively. Therefore, Eq. (23) can be rewritten as

$$\begin{aligned} \sigma_A: \mathbf{L}_A^e + \sigma_A: F_A^e \bar{L}_A^p (F_A^e)^{-1} + \sigma_B: \mathbf{L}_B - \nabla \cdot \mathbf{q} + \rho \dot{\phi} = \\ \sigma_A: \mathbf{D}_A^e + \sigma_B: \mathbf{D}_B - Y\dot{D} - \frac{1}{2} \frac{\partial((F_A^e)^{-1} \sigma_A (F_A^e)^{-T})}{\partial T} : \dot{C}_A^e - \frac{1}{2} \frac{\partial(F_B^{-1} \sigma_B F_B^{-T})}{\partial T} : \dot{C}_B + T \frac{\partial Y}{\partial T} \dot{D} - \rho T \frac{\partial^2 \psi}{\partial T^2} \dot{T}. \end{aligned} \tag{24}$$

Using the equations $\sigma_A: \mathbf{D}_A^e = \sigma_A: \mathbf{L}_A^e$ and $\sigma_B: \mathbf{L}_B = \sigma_B: \mathbf{D}_B$, the heat equation is thus obtained as

$$\rho c \dot{T} = \sigma_A: F_A^e \bar{L}_A^p (F_A^e)^{-1} + Y\dot{D} + \frac{1}{2} \frac{\partial((F_A^e)^{-1} \sigma_A (F_A^e)^{-T})}{\partial T} : \dot{C}_A^e + \frac{1}{2} \frac{\partial(F_B^{-1} \sigma_B F_B^{-T})}{\partial T} : \dot{C}_B - T \frac{\partial Y}{\partial T} \dot{D} - \nabla \cdot \mathbf{q} + \rho \dot{\phi}, \tag{25}$$

where the specific heat capacity $c = -T \partial^2 \psi / \partial T^2$ is used to simplify the equation. The two terms $\sigma_A: F_A^e \bar{L}_A^p (F_A^e)^{-1}$ and $Y\dot{D}$ represent the viscoplastic energy dissipation and the damage energy dissipation, respectively. The following three terms, namely $\frac{1}{2} \partial((F_A^e)^{-1} \sigma_A (F_A^e)^{-T}) / \partial T : \dot{C}_A^e$ and $\frac{1}{2} \partial(F_B^{-1} \sigma_B F_B^{-T}) / \partial T : \dot{C}_B$ representing the effect of the thermo-mechanical coupling on the self-heating and $-T \partial Y / \partial T$ representing the thermo-damage coupling, are not considered in the present study; this is because they are much smaller than the first two terms. By using $\mathbf{q} = -k \nabla T$ and ignoring the external heat source term $\rho \dot{\phi}$, Eq. (25) can be reduced to

$$\rho c \dot{T} = k \nabla \cdot (\nabla T) + \sigma_A: F_A^e \bar{L}_A^p (F_A^e)^{-1} + Y\dot{D}, \tag{26}$$

where k is the thermal conductivity. The last two terms can be regarded as the heat source terms associated with deformation.

2.4. Cauchy stresses

The specific Helmholtz free energy is defined to obtain the Cauchy stresses in the two branches. It can be decomposed into two independent components:

$$\psi = \psi_A(\mathbf{C}_A^c, D, T) + \psi_B(\mathbf{C}_B, D, T). \tag{27}$$

It is assumed that these two branches share the same damage. For branch A, the Cauchy stress is calculated according to the stretch of the linear spring. Therefore, the Helmholtz free energy of this branch is given as

$$\rho\psi_A = \frac{(1-D)}{J_A^c} \left[\mu(T) \ln \mathbf{U}_A^c : \ln \mathbf{U}_A^c + \frac{1}{2} \lambda(T) (\text{tr}(\ln \mathbf{U}_A^c))^2 \right], \tag{28}$$

where $J_A^c = \det(\mathbf{F}_A^c)$, \mathbf{U}_A^c is the stretch tensor obtained through the polar decomposition $\mathbf{F}_A^c = \mathbf{R}_A^c \mathbf{U}_A^c$, $\ln \mathbf{U}_A^c$ is the logarithmic strain, and the symbol $\text{tr}(\ln \mathbf{U}_A^c)$ represents the trace of the logarithmic strain.

According to Eq. (15), the Cauchy stress in branch A can be written as

$$\boldsymbol{\sigma}_A = \frac{(1-D)}{J_A^c} \mathbf{R}_A^c [2\mu(T) \ln \mathbf{U}_A^c + \lambda(T) \text{tr}(\ln \mathbf{U}_A^c) \mathbf{I}] (\mathbf{R}_A^c)^T, \tag{29}$$

where \mathbf{R}_A^c is the rotation tensor, μ and λ are temperature-dependent Lamé parameters. The detailed derivation is presented in Appendix A. The elastic properties E and ν are used instead of the Lamé parameters. The correlation between the elastic modulus and the temperature is given as:

$$E(T) = E_{\text{ref}} + E_s(T - T_{\text{ref}}), \tag{30}$$

where E_{ref} is the reference modulus under temperature T_{ref} and E_s is the slope of the linear relationship.

For branch B, a specific Helmholtz free energy is proposed through including damage in the eight-chain model (Arruda and Boyce, 1993; Dupaix and Boyce, 2007; Mulliken and Boyce, 2006; Qi and Boyce, 2004, 2005) to describe the strain hardening at large deformation:

$$\rho\psi_B = \frac{(1-D)}{J_B} C_r(T) \left(\sqrt{N} \bar{\lambda}_{\text{chain}} \beta + N \ln \frac{\beta}{\sinh \beta} \right), \tag{31}$$

where $J_B = \det(\mathbf{F}_B)$, the isochoric left Cauchy–Green tensor of this branch is $\bar{\mathbf{B}}_B = J_B^{-2/3} \mathbf{F}_B \mathbf{F}_B^T$, $\bar{I}_1 = \text{tr}(\bar{\mathbf{B}}_B)$ is the first invariant of $\bar{\mathbf{B}}_B$, the chain stretch of the eight-chain network is $\bar{\lambda}_{\text{chain}} = \sqrt{\bar{I}_1/3}$, $\beta = \text{La}^{-1}(\bar{\lambda}_{\text{chain}}/\sqrt{N})$, the symbol La is the Langevin function, the material parameter C_r represents the rubbery modulus and the parameter \sqrt{N} is the limit of the chain extensibility. The Cauchy stress in branch B is obtained according to Eq. (16) as

$$\boldsymbol{\sigma}_B = \frac{(1-D)}{J_B} \frac{C_r(T)}{3} \frac{\sqrt{N}}{\bar{\lambda}_{\text{chain}}} \text{La}^{-1} \left(\frac{\bar{\lambda}_{\text{chain}}}{\sqrt{N}} \right) \mathbf{B}'_B, \tag{32}$$

where \mathbf{B}'_B is the deviatoric part of $\bar{\mathbf{B}}_B$, $\mathbf{B}'_B = \bar{\mathbf{B}}_B - 1/3 \text{tr}(\bar{\mathbf{B}}_B) \mathbf{I}$.

According to Eq. (17), the damage energy release rate is calculated as

$$Y = \frac{1}{J_A^c} \left[\mu(T) \ln \mathbf{U}_A^c : \ln \mathbf{U}_A^c + \frac{1}{2} \lambda(T) (\text{tr}(\ln \mathbf{U}_A^c))^2 \right] + \frac{1}{J_B} C_r(T) \left(\sqrt{N} \bar{\lambda}_{\text{chain}} \beta + N \ln \frac{\beta}{\sinh \beta} \right). \tag{33}$$

The variable Y is used to calculate the damage energy dissipation in the heat equation.

2.5. Viscoplastic evolution

Based on an original form without damage (Kolupaev et al., 2005; Zerbe et al., 2017), a plastic dissipation potential including damage is proposed to describe the viscoplastic flow in branch A:

$$\varphi_p = \frac{1}{1-D} \sqrt{(1-\chi)\tau_A^2 + \chi(\text{tr}(\boldsymbol{\sigma}_A))^2}, \tag{34}$$

where the equivalent shear stress $\tau_A = \sqrt{3\boldsymbol{\sigma}'_A : \boldsymbol{\sigma}'_A/2}$ is obtained from the deviatoric stress $\boldsymbol{\sigma}'_A$, the symbol $\langle \rangle$ is the Macaulay bracket and χ is the material parameter controlling the contribution of the hydrostatic stress of $\boldsymbol{\sigma}_A$. The equivalent shear stress and the hydrostatic stress are both considered in the dissipation potential. The additional term $(1-D)$ in the equation considers the effect of damage on the viscoplastic deformation. The derivation of the plastic dissipation potential with respect to $\boldsymbol{\sigma}_A$ is given as

$$\frac{\partial \varphi_p}{\partial \boldsymbol{\sigma}_A} = \frac{3(1-\chi)\boldsymbol{\sigma}'_A + 2\chi\langle \text{tr}(\boldsymbol{\sigma}_A) \rangle \mathbf{I}}{2(1-D)\sqrt{(1-\chi)\tau_A^2 + \chi(\text{tr}(\boldsymbol{\sigma}_A))^2}}. \tag{35}$$

The viscoplastic evolution rule is thus obtained according to Eqs. (19) and (20).

The viscoplastic multiplier $\dot{\lambda}_p$ is controlled by the Cauchy stress acting on the viscoplastic dashpot (Torres et al., 2016):

$$\dot{\lambda}_p = \dot{\lambda}_0 \left(\frac{\tau_A}{\sigma_y(T)f_p} \right)^m, \tag{36}$$

where σ_y is the temperature-dependent shear resistance, $\dot{\lambda}_0$ is a material constant and m is the strain rate sensitivity parameter. The function f_p is used to capture the nonlinear yielding behavior:

$$f_p = \delta + (1 - \delta)\exp\left(-\frac{p}{p_y}\right), \tag{37}$$

where δ and p_y are material parameters. The rate of the equivalent viscoplastic strain p is given as

$$\dot{p} = \sqrt{\frac{2}{3} \mathbf{F}_A^e \bar{\mathbf{L}}_A^p (\mathbf{F}_A^e)^{-1} : \mathbf{F}_A^e \bar{\mathbf{L}}_A^p (\mathbf{F}_A^e)^{-1}}. \tag{38}$$

2.6. Damage evolution

The damage rate is proposed as an exponent function of the equivalent viscoplastic strain:

$$\dot{D} = D_c \beta \exp(-\beta p) \dot{p}, \tag{39}$$

where β is a material parameter controlling the evolution of damage and D_c is the damage limit. Through the integration of Eq. (39), the damage model can be written as

$$D = D_c (1 - \exp(-\beta p)), \tag{40}$$

where zero damage at the initial condition is assumed. This equation is used to determine the damage parameters D_c and β . The damage rate Eq. (39) will be used in conjunction with the viscoplastic evolution law to calculate the evolution of damage and viscoplastic deformation gradient.

2.7. Numerical implementation

The proposed model is implemented in the finite element code ABAQUS by using the explicit subroutine VUMAT. Three procedures are performed to calculate the Cauchy stresses, viscoplastic deformation gradient, damage and temperature:

- a) The differential equations in the viscoplastic and damage evolution model are solved by an explicit Runge-Kutta procedure to obtain the viscoplastic deformation gradient \mathbf{F}_A^p , damage D and equivalent viscoplastic strain p .
- b) Two deformation gradients \mathbf{F}_A^e and \mathbf{F}_B are then prepared for the calculation of the two Cauchy stresses. An incremental method is applied because the damage and the deformation gradient are changing gradually. Especially, the increment of the elastic deformation gradient at the current step is given as

$$\Delta \mathbf{F}_A^e = \mathbf{F}_{A,c}^e (\mathbf{F}_{A,l}^e)^{-1}, \tag{41}$$

where $\mathbf{F}_{A,c}^e$ and $\mathbf{F}_{A,l}^e$ represent the elastic deformation gradients at the current and previous time step, respectively. The elastic strain increment is thus calculated as

$$\mathbf{D}_A^e \Delta t = \frac{1}{2} (\mathbf{I} - (\Delta \mathbf{F}_A^e)^{-T} (\Delta \mathbf{F}_A^e)^{-1}). \tag{42}$$

The stress at the current step is obtained from the results of elastic strain increment, damage and temperature at the previous step.

- c) The temperature increment is calculated by providing the two energy dissipation terms $\sigma_A : \mathbf{F}_A^e \bar{\mathbf{L}}_A^p (\mathbf{F}_A^e)^{-1} \Delta t$ and $Y \dot{D} \Delta t$ in Eq. (26).

The procedures are repeated until the end of the simulation. After each step, the results of stress, viscoplastic deformation gradient, damage and temperature are updated as the initial condition for the next step.

3. Parameter calibration for polyamide 6

The material studied is a semi-crystalline polyamide 6. The specimens are machined from 3 mm thick plate (purchased from Nai Mei Hardware Product Co., Ltd., Shenzhen, China). They have a dog-bone shape and 8 mm-width reduced section. The stress-strain behavior and the damage evolution of polyamide 6 are investigated through monotonic loading tests and repeated loading tests, respectively. The experimental results from both tests are used to calibrate the material parameters in the developed model.

3.1. Monotonic loading tests

Monotonic tensile tests are conducted to evaluate the stress-strain responses of polyamide 6 under different loading conditions. Three temperatures (25, 50 and 80 °C) and three loading rates (1, 10 and 100 mm/min) are used in the tests. The specimens in a temperature chamber are heated up to the testing temperature prior to the tensile tests. The thermal strain and stress due to heating are eliminated by adjusting the initial clamp position of the testing machine before the test. Two black lines are marked on the reduced section of the specimen and the distance between them is recorded as the gauge length. One end of the specimen is fixed by the lower clamp of the testing machine. The displacement with a specific loading rate is applied on the other end of the specimen through the upper clamp. The deformation of a specimen in the chamber is measured by a video extensometer (TRview X) that

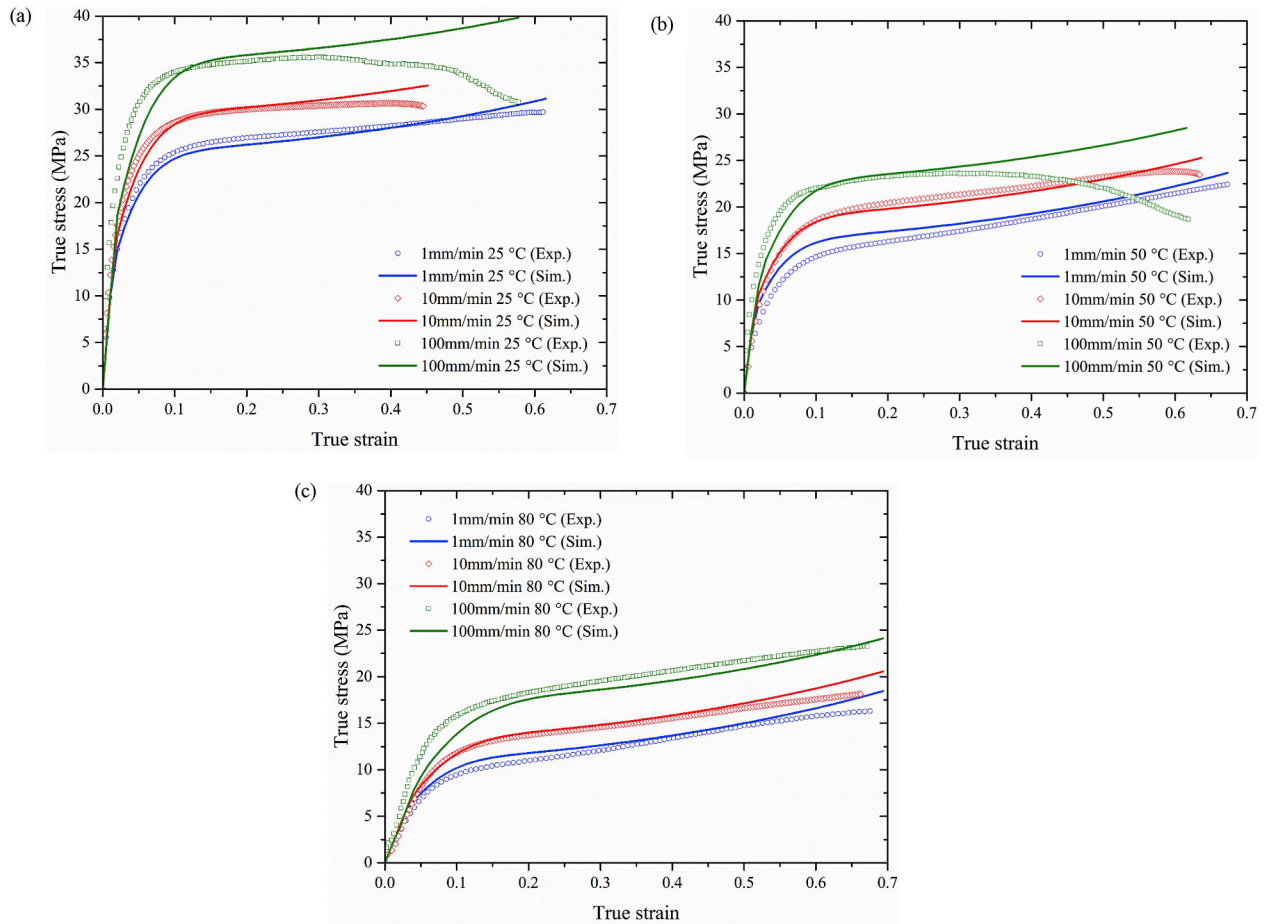


Fig. 3. Experimental and numerical results of strain-strain curves of polyamide 6 under three loading rates (1, 10 and 100 mm/min) at three temperatures: (a) 25, (b) 50 and (c) 80 °C.

captures movements of these two lines on the specimen. The obtained strain is thus an average over the region bounded by the lines. The forces during the tests are recorded to calculate the stresses under different loading conditions.

Fig. 3 depicts the stress-strain responses of polyamide 6 for three loading rates at three different temperatures. All experimental curves start with linear elastic behavior at small deformation, i.e., the strain is less than around 0.02. Then nonlinear yielding stages are observed in the strain range from 0.02 to 0.15. The stress slightly increases (i.e., strain hardening) as the strain is larger than around 0.15. However, necking occurs under 100 mm/min loading rate at two temperatures, namely 25 and 50 °C. The stress reduction under both loading conditions is significant as the strain is larger than 0.3. It is noted that the deformation at this stage is inhomogeneous due to necking.

The loading rate significantly affects the yielding behavior of polyamide 6. Higher loading rate causes larger stress after the initial elastic stage. However, the initial yield stresses are nearly identical for the three loading rates at each temperature. Furthermore, the hardening rate at the last stage is slightly influenced by the loading rate. The temperature affects the initial elastic modulus and nonlinear yielding behavior. The stress at a strain of 0.2 under the loading rate of 1 mm/min decreases from around 27 to 11 MPa as the testing temperature increases from 25 to 80 °C. High temperature leads to low elastic modulus and initial yield stress.

It is noted that the glass-rubber transition temperature of polyamide 6 is around 50 °C. The chosen three testing temperatures span the glass-rubber transition of this material. However, the stress-strain curves under these three temperatures have similar features including initial elastic behavior and subsequent viscoplastic behavior. No distinct difference can be observed. Therefore, the effect of the glass-rubber transition on the thermo-mechanical behavior is not obvious for polyamide 6.

3.2. Repeated loading tests

The repeated loading tests are used to investigate the damage evolution of polyamide 6. A deformed specimen is unloaded and then reloaded to a larger deformation. The variation of the mechanical behavior is unveiled through multiple unloading-loading processes. For metallic materials, the unloading process usually exhibits linear elasticity and the elastic modulus is the slope of the unloading curve (Walvekar et al., 2014). However, the unloading curve of thermoplastic polymers is more complex with obvious

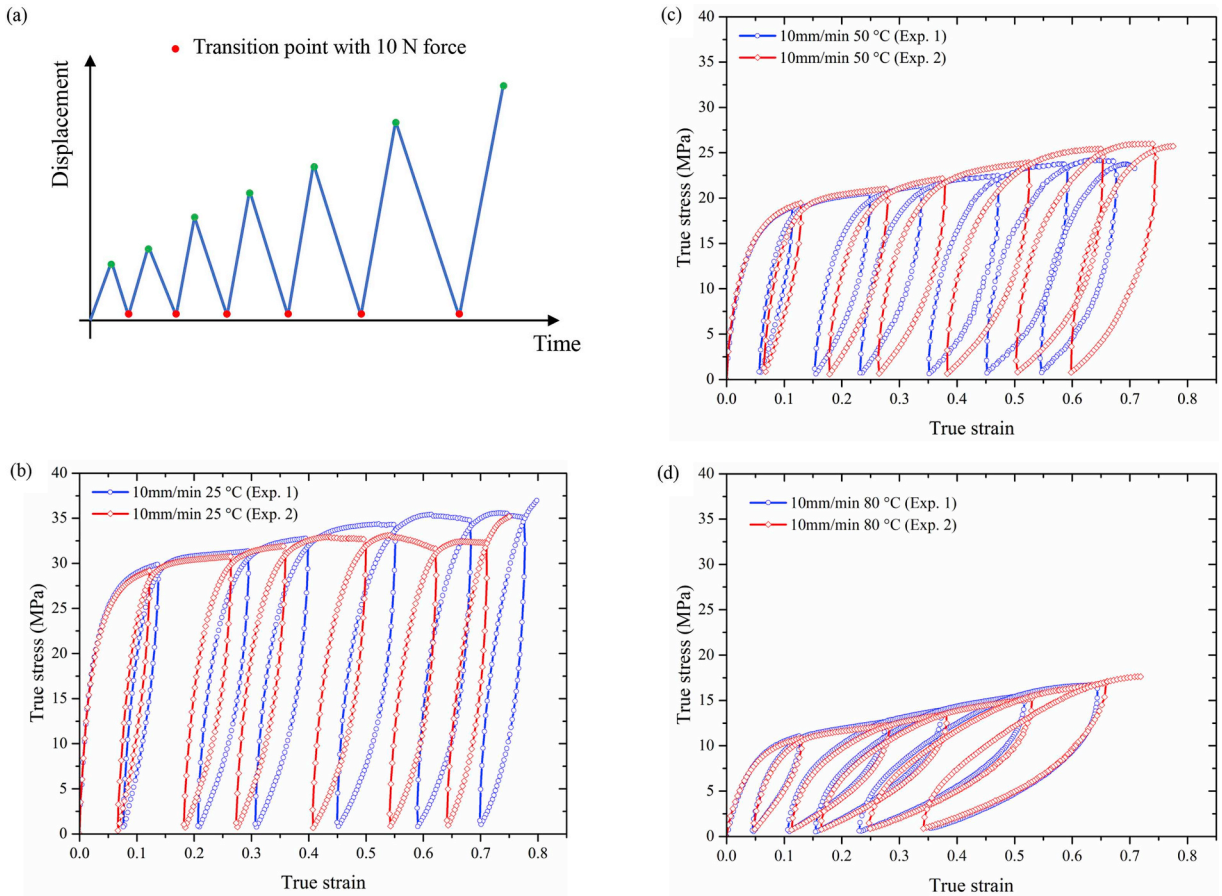


Fig. 4. (a) Schematic of applied displacement history in repeated loading tests. Stress-strain curves of polyamide 6 under 10 mm/min loading rate at three temperatures: (b) 25, (c) 50 and (d) 80 °C.

nonlinearities and hysteresis loops. Balieu et al. (2013) proposed a method to calculate the stiffness by using two points at the top-right and bottom-left corners in the hysteresis loop. The non-damaged stiffness is determined from the elastic portion of the stress-strain curve. The damage evolution is then calculated according to the damaged stiffness and the non-damaged stiffness.

The repeated loading tests are conducted under 10 mm/min loading rate at three temperatures. The damage evolution results under this moderate loading rate are used in the developed model to reproduce the stress-strain behavior under these three loading rates. The higher loading rate of 100 mm/min is not used because of specimen necking. The thermostatic chamber in the monotonic tests is also used in the repeated loading tests. Fig. 4(a) shows the schematic of displacement history applied on the specimens in repeated loading tests. For each test, several unloading-loading processes are performed to obtain hysteresis loops at different strains. The end of the loading process is controlled by the applied displacement. The maximum displacements in these processes are given as 3, 7, 10, 15, 20 and 24 mm. With significant plastic deformation, a compressive force will occur if the specimen is unloaded to zero displacement. Therefore, the specimen is unloaded to a state with a small tensile force of 10 N. As the force on the specimen decreases to this value, the unloading process is terminated and a loading process commences.

Fig. 4(b)-(d) display the stress-strain curves under 10 mm/min loading rate at three different temperatures. Two specimens are used at each temperature. The applied displacements for these two specimens are identical. The discrepancies between their stress-strain responses are mainly caused by their slightly different gauge lengths. With this arrangement, more data points at each testing temperature can be obtained. Furthermore, the scattering of mechanical properties of the specimens induced in the manufacturing process also contributes to the discrepancies.

The shapes and sizes of the hysteresis loops evolve with increasing strain. The loops rotate gradually in a clockwise direction as the strain increases, indicating the weakening of material properties. Furthermore, the loop size grows larger, which means that more energy is dissipated in the unloading-loading process. The envelopes of the stress-strain curves are consistent with the curves obtained in the monotonic loading tests, indicating the testing repeatability on the mechanical behavior of the polymer. At 80 °C, the force cannot decrease to 10 N at the end of the testing to trigger the status change from unloading to loading for the first specimen. In addition, the displacement of 24 mm is not reached for the second specimen. Therefore, the number of hysteresis loops under this temperature is less than those for other two temperatures.

Fig. 5 shows the damages calculated based on the information of hysteresis loops at these three temperatures. The plastic strain of

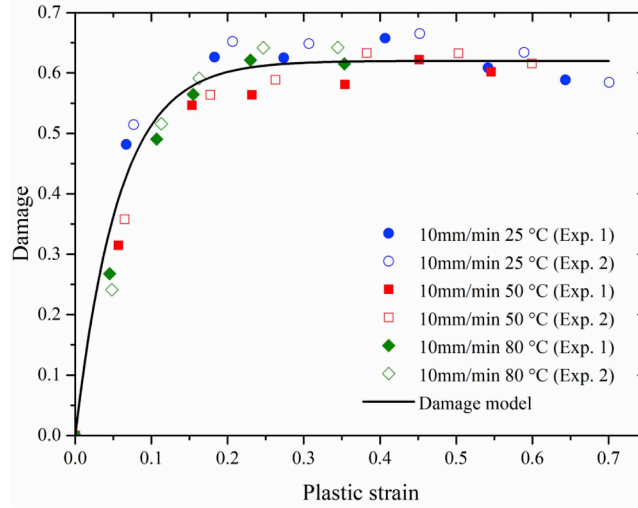


Fig. 5. Experimental and model results of damage evolution of polyamide 6 under 10 mm/min loading rate at three different temperatures.

each damage point is the residual strain at the end of the unloading process. Damage increases rapidly as the plastic strain is less than 0.1 and then its increment rate slows down gradually. A damage plateau is reached as the plastic strain is larger than 0.2. Even though temperature affects the shapes and sizes of the hysteresis loops, the damage values at the plateaus under these three temperatures fall in a relatively narrow range from 0.57 to 0.66. No clear distinction can be observed among these three groups of damage data.

3.3. Parameter calibration procedure

The material parameters in the developed thermo-elastic-viscoplastic-damage model can be classified into five categories: E_s , E_{ref} , ν and T_{ref} in the stress calculation of branch A; C_r and N in the stress calculation of branch B; σ_y , $\dot{\lambda}_0$, m , χ , δ and p_y in the viscoplastic evolution model; D_c and β in the damage evolution model; ρ , c and k in the heat equation.

The stress-strain curves in the monotonic loading tests are used to calibrate the material parameters in the first three categories. It is noted that tests with specimen necking are not suitable for the parameter calibration. Therefore, only seven groups of testing results are used to determine the parameters. The elastic moduli under 10 mm/min loading rate at three different temperatures are determined from the elastic stages of stress-strain curves. Two parameters E_s and E_{ref} are obtained based on the relationship between the elastic moduli and temperatures. The reference temperature is set as $T_{ref} = 25^\circ\text{C}$. The Poisson's ratio is set as $\nu = 0.4$. The parameter σ_y can be determined as the initial yield stress beyond the elastic stage, which exhibits a linear relationship to the temperature:

$$\sigma_y(T) = \sigma_{yref} + \sigma_{ys}(T - T_{ref}), \tag{43}$$

where σ_{yref} and σ_{ys} are two material parameters. For parameters $\dot{\lambda}_0$, m , δ , p_y and χ in the viscoplastic flow equation, a numerical procedure is needed to determine them. One 8-node coupled thermo-mechanical element with unit dimensions is built in the finite element code ABAQUS to predict the stress-strain behavior of the polymer. Uniaxial tensile displacement controlled by the loading rate is applied on the element. The element temperature is given according to the experimental condition in each monotonic test. The calibration procedure for material parameters $\dot{\lambda}_0$, m , δ , p_y and χ is based on the comparison between the numerical stress responses and the experimental results in the monotonic loading tests (two necking cases are not included). The obtained parameters need to minimize the ratio of the least square residual to the sum of squares of the experimental stresses (Maurel-Pantel et al., 2015; Polanco-Loria et al., 2012):

$$R_{error} = \sqrt{\frac{\sum_{i=1}^n (\sigma_i(\epsilon_i)_{exp.} - \sigma_i(\epsilon_i, X)_{sim.})^2}{\sum_{i=1}^n (\sigma_i(\epsilon_i)_{exp.})^2}}, \tag{44}$$

where the symbol $X = [\dot{\lambda}_0, m, \delta, p_y, \chi]$ is the variables to be determined. C_r and N are obtained from the curves at large strain ranging from 0.2 to 0.5. As the temperature has an insignificant influence on the hardening behavior in this strain range, a temperature-independent parameter C_r is assumed. The parameters D_c and β are determined from the results of damage evolution obtained from the repeated loading tests. As shown in Fig. 5, an average damage value of 0.62 is used as the damage limit at these three temperatures. The maximum relative error between the experimental results and this average value is about 6%. Since the maximum temperature increase is around 25 °C, the physical properties ρ , c and k are assumed to be temperature-independent. The model parameters and thermal properties for polyamide 6 are listed in Table 1.

The stress-strain curves of isothermal monotonic tests are obtained after the calibration of the material parameters, as shown in

Table 1
Model parameters and thermal properties for polyamide 6.

Elastic properties				Strain hardening		
E_{ref} (MPa)	E_s (MPa/°C)	ν	T_{ref} (°C)	C_r (MPa)	N	
967	−14.4	0.4	25	6	9.17	
Viscoplastic flow						
σ_{yref} (MPa)	σ_{ys} (MPa/°C)	$\dot{\lambda}_0$	m	δ	P_y	χ
15.0	−0.22	0.0015	15.0	0.9	0.03	0.19
Damage evolution			Thermal properties			
D_c	β	ρ (kg/m ³)	c (J/(kg °C))	k (W/(m °C))		
0.62	17.61	1140	1700	0.28		

Fig. 3. The calibration differences R_{error} for seven groups of monotonic testing results are presented in Table 2. The maximum difference is around 0.3%, indicating that an excellent agreement between the experimental and simulation results is achieved. Therefore, the proposed model can reproduce the stress-strain behavior of polyamide 6 under tensile loading; these include the initial elasticity, the nonlinear viscoplastic flow at moderate deformation and the strain hardening at large deformation under different temperatures and loading rates. Furthermore, the damage evolution during deformation and its influence on the mechanical behavior in the three stages are also considered in the model.

A discrepancy between the experimental and simulation curves is observed under two loading conditions (i.e., 100 mm/min 25 °C and 100 mm/min 50 °C), especially at the last stage of deformation. Necking occurs in both cases as the strain is larger than 0.3. This discrepancy may be attributed to the inhomogeneous deformation in the necking zone. The measured stress decreases significantly after the onset of necking. However, the one-element modeling represents uniform deformation and thus the predicted stress continues to increase.

4. Model validation

The self-heating tests are conducted to investigate the mechanical behavior and temperature evolution of polyamide 6 under a high loading rate. In conjunction with the finite element method, the developed model is used to predict the thermo-mechanical response in the self-heating tests. The model is validated through the comparison between the numerical and experimental results.

4.1. Self-heating tests

The self-heating behavior during monotonic loading is measured through an infrared camera (FLIR system) at room temperature. The surfaces of the specimen are painted black to have the surface emissivity close to unity. In addition, before the actual tests, temperature calibration at the testing condition is conducted to ensure the accuracy of temperature measurements. No temperature chamber is required in the tests. The loading rate of 120 mm/min is used in the tensile tests until specimen necking occurred. The temperature evolution on the specimen surface is captured at a sampling frequency of 20 Hz.

Fig. 6 illustrates the evolution of the increment of maximum temperature and the tensile force in terms of deformation time. Necking initiates in the reduced section of the specimen, with a distance of around 22 mm from the bottom clamp. The maximum temperature occurs in the necking zone during the self-heating tests. Its position varies over time due to the increase in the length of the necking zone. However, the exact position of the maximum temperature in the necking zone is not measured in the tests. Temperature exhibits a significant increase in the first 12 s, and then comes to a plateau with a maximum increment of around 25 °C. A slight decrease in the temperature is observed in the plateau. The tensile force increases rapidly and reaches the maximum at 3.5 s.

Table 2
Material parameter calibration errors for seven groups of monotonic tests.

Temperature (°C)	Loading rate (mm/min)	R_{error} (%)
25	1	0.052
	10	0.11
50	1	0.28
	10	0.079
80	1	0.30
	10	0.2
	100	0.28

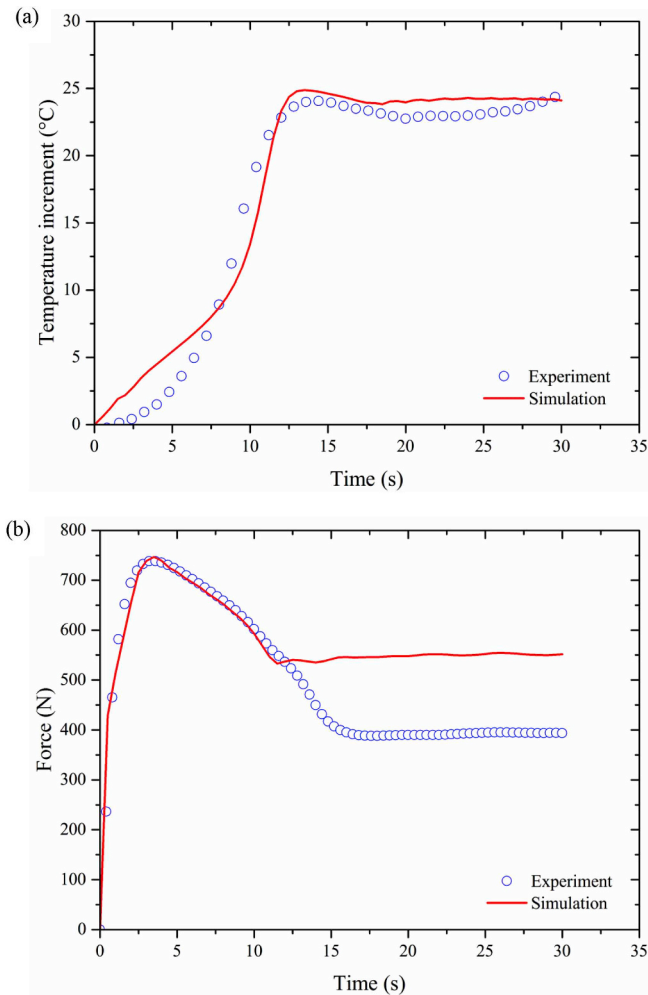


Fig. 6. In terms of deformation time for polyamide 6 at 120 mm/min loading rate and room temperature, experimental and numerical results of the evolution of (a) the increment of maximum temperature and (b) the tensile force.

After that it begins to decrease, indicating the onset of specimen necking. However, necking is not obvious until approximately 10 s. The force finally becomes constant after around 15 s.

4.2. Finite element simulation

The finite element model of the testing specimen is established in ABAQUS according to the specimen dimensions. The 8-node

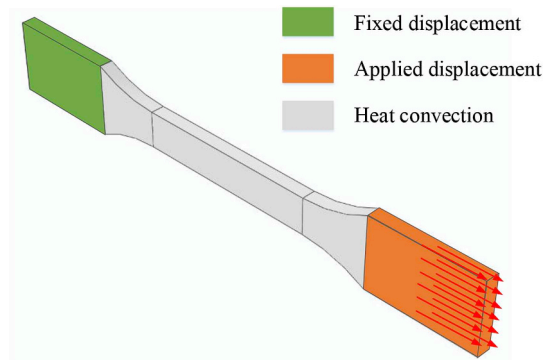


Fig. 7. Mechanical and thermal boundary conditions on the specimen.

coupled thermo-mechanical elements are used. One end of the specimen clamped by the testing machine is fixed and a tensile displacement is applied on the other end of the specimen, as shown in Fig. 7. The environment temperature is set as the room temperature in the self-heating tests. The heat convection boundary condition is given on the surfaces of the specimen:

$$\mathbf{n}(k\nabla T) = h(T - T_{env}), \quad (45)$$

where the vector \mathbf{n} represents the normal direction of a specimen surface. The convection coefficient $h = 25 \text{ W}/(\text{m}^2 \text{ }^\circ\text{C})$ is used in the modeling (Bai et al., 2015; Shen et al., 2018). A geometrical imperfection is set on the specimen to provide the initiation position of necking.

4.3. Model validation

The self-heating tests under 120 mm/min loading rate at room temperature are simulated by the developed model to predict the self-heating and mechanical behavior of polyamide 6. The predicted results of the temperature increment and the load evolution curves are compared with the experimental data. The temperature increase stage and the temperature plateau stage are reproduced by using the developed model, see Fig. 6(a). The predicted time reaching the plateau is consistent with the experimental result. The maximum difference between the temperature increments obtained from the testing and modeling is around 3.3%. The proposed model can provide an accurate prediction of the load evolution in the first 10 s. However, the predicted load at the last stage of the deformation deviates from the testing result as shown in Fig. 6(b). The predicted final stable stage occurs earlier than the experimental results. It indicates the limitation of the developed model in predicting the final stable stage of necking.

Fig. 8(a) and (b) illustrate the predicted damage and temperature distributions on the specimen surface at three time instances, namely 3.5, 10 and 15 s. The two clamped ends of the specimen by the testing machine are not shown in this figure. The stress concentration occurs in the section with the geometrical imperfection. It causes a localized increase of the damage, and thus the temperature under tensile loading. At 3.5 s, significant damage up to around 0.5 is localized in the entire cross section. Furthermore, the temperature of this section is higher than those of other regions. The maximum temperature increment is around 4 °C. The material weakening due to the damage and temperature rise causes a significant increase of the strain in the section. However, the contribution of damage is much larger than that of thermal softening. After this time, the predicted tensile load begins to decrease even though the specimen is still stretched. Necking is clearly visible after around 10 s, which agrees well with the experimental observation. The increment of the surface temperature is significant in the necking section due to the huge plastic deformation. The damage distribution in the reduced section becomes uniform at 10 s because the damage for all the materials reaches the limit D_c . Fig. 8(c) shows the experimental observations of the surface temperature distributions at three time instances. By comparing the experimental and predicted results, excellent agreements on the temperature evolution have been achieved.

Fig. 9 shows the evolutions of the viscoplastic and damage energy accumulations for the material in the necking section. It is noted that the energy accumulation is the summation of the dissipated energies at all time steps rather than the energy dissipation at the current step. The variation of the damage energy accumulation is similar to the damage evolution determined in the repeated loading tests. A limit of the damage energy accumulation is reached after about 6 s. After that, the contribution of damage on self-heating vanishes because the damage is unchanged. However, the viscoplastic energy accumulation still increases because of specimen necking. It reaches a plateau with a maximum value of around 48 MPa after 15 s. The energy dissipated in the viscoplastic deformation is about one order larger than the damage energy. Therefore, the viscoplastic energy dissipation is the dominant heat source for causing the significant increase of temperature after the onset of specimen necking.

5. Conclusions

The thermo-mechanical behavior of polyamide 6 consists of three stages: the initial temperature-dependent elastic behavior, the nonlinear yielding with temperature and loading rate dependencies, and the strain hardening at large strain.

Self-heating and mechanical behavior including the damage evolution at large deformation of polyamide 6 are experimentally investigated through three types of tests. The monotonic loading tests are conducted to evaluate the stress-strain responses at different temperatures and loading rates. The repeated loading tests under different temperatures are performed to evaluate the damage evolution described by the reduction of material stiffness. The self-heating tests are performed to capture the temperature evolution of specimens at high loading rate.

The influence of temperature on damage evolution is investigated. The damage at each temperature starts with a rapid increase and then reaches a plateau. No clear distinction can be observed among the damage data under the three temperatures investigated. The temperature evolution after the onset of necking is obvious in the self-heating tests and the large temperature increment localizes in the necking zone.

A thermo-elastic-viscoplastic-damage model is developed within the thermodynamic framework to interpret the temperature evolution and thermo-mechanical behavior of polyamide 6 at large deformation. The relationships between stress, strain, damage, temperature and loading rate are considered in the model. The temperature evolution is evaluated through consideration of energy dissipation from both the viscoplastic deformation and the damage process. The model parameters are calibrated from the results of the monotonic and repeated loading tests. The proposed model is then used to predict the temperature evolution and mechanical response in the self-heating tests. The predicted results of temperature increment and load evolution agree well with the experimental data.

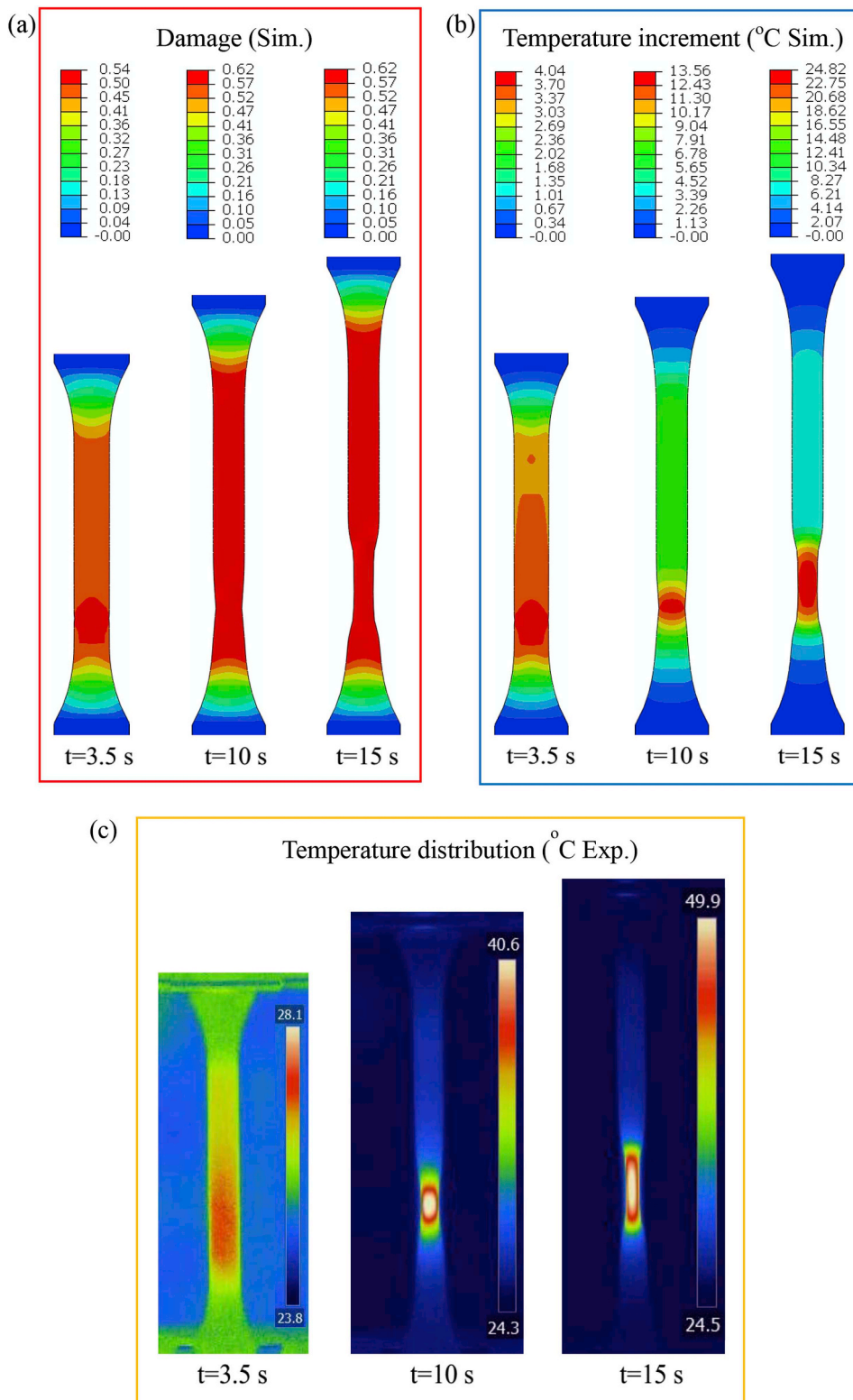


Fig. 8. Distributions of (a) predicted damage, (b) predicted temperature increment and (c) measured temperature on the specimen surface at 3.5, 10 and 15 s.

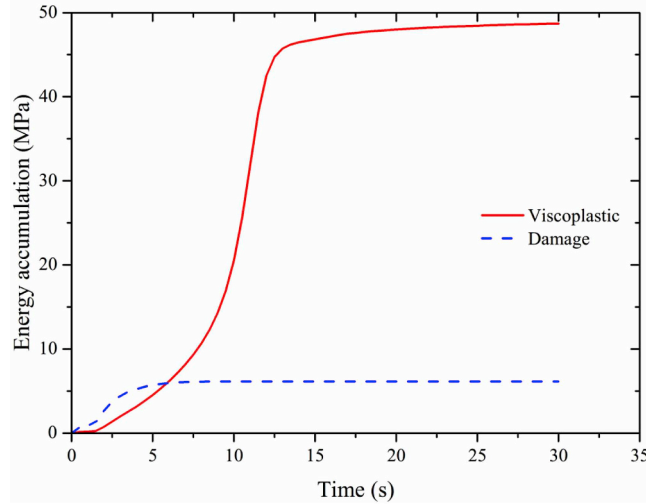


Fig. 9. Evolutions of the viscoplastic and damage energy accumulation with respect to time for a material point in the necking section.

Acknowledgments

The authors acknowledge the financial support from the SMRT-NTU Smart Urban Rail Corporate Lab, Singapore. K. Z. acknowledges the financial support from the Nanyang Environment and Water Research Institute (Core Fund), Nanyang Technological University, Singapore.

Appendix A. Derivation of Cauchy stress in branch A

The Cauchy stress in the intermolecular resistance is derived through Eqs. (15) and (28). To calculate the derivative of $\ln \mathbf{U}_A^c$ with respect to \mathbf{C}_A^e , the Helmholtz free energy $\rho\psi_A$ is described by the principal elastic logarithmic strain (Bouvard et al., 2013):

$$\rho\psi_A = \frac{(1-D)}{J_A^e} \left[\mu(T) \sum_{i=1}^3 h_i^2 + \frac{1}{2} \lambda(T) \left(\sum_{i=1}^3 h_i \right)^2 \right], \tag{A1}$$

where the logarithm strain is defined as $h_i = \ln \gamma_i$ and γ_i is the principal stretch of \mathbf{U}_A^e . The Cauchy stress is expressed as

$$\sigma_A = 2\mathbf{F}_A^e \rho \frac{\partial \psi_A}{\partial \mathbf{C}_A^e} \mathbf{F}_A^{eT} = 2\mathbf{F}_A^e \left(\rho \sum_{i=1}^3 \frac{\partial \psi_A(h_i)}{\partial h_i} \frac{\partial h_i}{\partial \gamma_i} \frac{\partial \gamma_i}{\partial \mathbf{C}_A^e} \right) \mathbf{F}_A^{eT} = \mathbf{R}_A^e \mathbf{U}_A^e \left(\rho \sum_{i=1}^3 \frac{1}{\gamma_i^2} \frac{\partial \psi_A(h_i)}{\partial h_i} \mathbf{e}_i \otimes \mathbf{e}_i \right) \mathbf{U}_A^e \mathbf{R}_A^{eT}, \tag{A2}$$

where \mathbf{e}_i is the unit eigenvector associated with the corresponding eigenvalue γ_i . The deformation \mathbf{U}_A^e and its logarithm is written as $\mathbf{U}_A^e = \sum_{i=1}^3 \gamma_i \mathbf{e}_i \otimes \mathbf{e}_i$ and $\ln \mathbf{U}_A^e = \sum_{i=1}^3 h_i \mathbf{e}_i \otimes \mathbf{e}_i$, respectively. By considering the term $\rho \sum_{i=1}^3 \frac{1}{\gamma_i^2} \frac{\partial \psi_A(h_i)}{\partial h_i} \mathbf{e}_i \otimes \mathbf{e}_i$ is coaxial with \mathbf{U}_A^e , Eq. (A2) can be rewritten as

$$\sigma_A = \mathbf{R}_A^e \left(\rho \sum_{i=1}^3 \frac{\partial \psi_A(h_i)}{\partial h_i} \mathbf{e}_i \otimes \mathbf{e}_i \right) \mathbf{R}_A^{eT} = \frac{(1-D)}{J_A^e} \mathbf{R}_A^e \left[2\mu(T) \sum_{i=1}^3 h_i \mathbf{e}_i \otimes \mathbf{e}_i + \lambda(T) \left(\sum_{i=1}^3 h_i \right) \sum_{i=1}^3 \mathbf{e}_i \otimes \mathbf{e}_i \right] \mathbf{R}_A^{eT} = \frac{(1-D)}{J_A^e} \mathbf{R}_A^e [2\mu(T) \ln \mathbf{U}_A^e + \lambda(T) \text{trace}(\ln \mathbf{U}_A^e) \mathbf{I}] \mathbf{R}_A^{eT}. \tag{A3}$$

References

Al-Rub, R.K.A., Voyiadjis, G.Z., 2003. On the coupling of anisotropic damage and plasticity models for ductile materials. *Int. J. Solids Struct.* 40, 2611–2643.
 Anand, L., Ames, N.M., Srivastava, V., Chester, S.A., 2009. A thermo-mechanically coupled theory for large deformations of amorphous polymers. Part I: Formulation. *Int. J. Plast.* 25, 1474–1494.
 Arruda, E.M., Boyce, M.C., 1993. A three-dimensional constitutive model for the large stretch behavior of rubber elastic materials. *J. Mech. Phys. Solids* 41, 389–412.
 Arruda, E.M., Boyce, M.C., Jayachandran, R., 1995. Effects of strain rate, temperature and thermomechanical coupling on the finite strain deformation of glassy polymers. *Mech. Mater.* 19, 193–212.
 Ayoub, G., Nait-Abdelaziz, M., Zaïri, F., Gloaguen, J.-M., Charrier, P., 2011a. A continuum damage model for the high-cycle fatigue life prediction of styrene-butadiene rubber under multiaxial loading. *Int. J. Solids Struct.* 48, 2458–2466.
 Ayoub, G., Zaïri, F., Nait-Abdelaziz, M., Gloaguen, J.M., 2011b. Modeling the low-cycle fatigue behavior of visco-hyperelastic elastomeric materials using a new network alteration theory: application to styrene-butadiene rubber. *J. Mech. Phys. Solids* 59, 473–495.
 Bai, J., Goodridge, R., Yuan, S., Zhou, K., Chua, C., Wei, J., 2015. Thermal influence of CNT on the polyamide 12 nanocomposite for selective laser sintering. *Molecules* 20, 19041–19050.
 Balieu, R., Lauro, F., Bennani, B., Delille, R., Matsumoto, T., Mottola, E., 2013. A fully coupled elastoviscoplastic damage model at finite strains for mineral filled semi-

- crystalline polymer. *Int. J. Plast.* 51, 241–270.
- Barentsen, W., Heikens, D., 1973. Mechanical properties of polystyrene/low density polyethylene blends. *Polymer* 14, 579–583.
- Bax, B., Müssig, J., 2008. Impact and tensile properties of PLA/Cordenka and PLA/flax composites. *Compos. Sci. Technol.* 68, 1601–1607.
- Belytschko, T., Liu, W.K., Moran, B., Elkhodary, K., 2013. *Nonlinear Finite Elements for Continua and Structures*. John Wiley & Sons.
- Bouvard, J.L., Francis, D.K., Tschopp, M.A., Marin, E.B., Bammann, D.J., Horstemeyer, M.F., 2013. An internal state variable material model for predicting the time, thermomechanical, and stress state dependence of amorphous glassy polymers under large deformation. *Int. J. Plast.* 42, 168–193.
- Boyce, M.C., Parks, D.M., Argon, A.S., 1988. Large inelastic deformation of glassy polymers. Part I: rate dependent constitutive model. *Mech. Mater.* 7, 15–33.
- Boyce, M.C., Arruda, E.M., Jayachandran, R., 1994. The large strain compression, tension, and simple shear of polycarbonate. *Polym. Eng. Sci.* 34, 716–725.
- Boyce, M., Socrate, S., Llana, P., 2000. Constitutive model for the finite deformation stress–strain behavior of poly (ethylene terephthalate) above the glass transition. *Polymer* 41, 2183–2201.
- Buckley, C., Jones, D., 1995. Glass-rubber constitutive model for amorphous polymers near the glass transition. *Polymer* 36, 3301–3312.
- Challier, M., Besson, J., Laiarinandrasana, L., Piques, R., 2006. Damage and fracture of polyvinylidene fluoride (PVDF) at 20 C: experiments and modelling. *Eng. Fract. Mech.* 73, 79–90.
- Chen, W., Lu, F., Cheng, M., 2002. Tension and compression tests of two polymers under quasi-static and dynamic loading. *Polym. Test.* 21, 113–121.
- Chen, K., Kang, G., Lu, F., Chen, J., Jiang, H., 2016. Effect of relative humidity on uniaxial cyclic softening/hardening and intrinsic heat generation of polyamide-6 polymer. *Polym. Test.* 56, 19–28.
- Detrez, F., Cantournet, S., Seguela, R., 2011. Plasticity/damage coupling in semi-crystalline polymers prior to yielding: micromechanisms and damage law identification. *Polymer* 52, 1998–2008.
- Dooling, P., Buckley, C., Rostami, S., Zahlan, N., 2002. Hot-drawing of poly (methyl methacrylate) and simulation using a glass–rubber constitutive model. *Polymer* 43, 2451–2465.
- Dupaix, R.B., Boyce, M.C., 2007. Constitutive modeling of the finite strain behavior of amorphous polymers in and above the glass transition. *Mech. Mater.* 39, 39–52.
- Garcia-Gonzalez, D., Zaera, R., Arias, A., 2017. A hyperelastic-thermoviscoplastic constitutive model for semi-crystalline polymers: application to PEEK under dynamic loading conditions. *Int. J. Plast.* 88, 27–52.
- Gurson, A.L., 1977. Continuum theory of ductile rupture by void nucleation and growth: Part I—yield criteria and flow rules for porous ductile media. *J. Eng. Mater. Technol.* 99, 2–15.
- Haddag, B., Abed-Meraim, F., Balan, T., 2009. Strain localization analysis using a large deformation anisotropic elastic–plastic model coupled with damage. *Int. J. Plast.* 25, 1970–1996.
- Hine, P.J., Duckett, R.A., Kaddour, A.S., Hinton, M.J., Wells, G.M., 2005. The effect of hydrostatic pressure on the mechanical properties of glass fibre/epoxy unidirectional composites. *Compos. Appl. Sci. Manuf.* 36, 279–289.
- Holopainen, S., Barriere, T., Cheng, G., Kouhia, R., 2017. Continuum approach for modeling fatigue in amorphous glassy polymers. Applications to the investigation of damage-ratcheting interaction in polycarbonate. *Int. J. Plast.* 91, 109–133.
- Jabbari-Farouji, S., Rottler, J., Lame, O., Makke, A., Perez, M., Barrat, J.-L., 2015. Plastic deformation mechanisms of semicrystalline and amorphous polymers. *ACS Macro Lett.* 4, 147–150.
- Jeong, H.-Y., Pan, J., 1995. A macroscopic constitutive law for porous solids with pressure-sensitive matrices and its implications to plastic flow localization. *Int. J. Solids Struct.* 32, 3669–3691.
- Kennedy, M., Peacock, A., Mandelkern, L., 1994. Tensile properties of crystalline polymers: linear polyethylene. *Macromolecules* 27, 5297–5310.
- Kolupaev, V., Moneke, M., Darsow, N., 2005. Modelling of the three-dimensional creep behavior of non-reinforced thermoplastics. *Comput. Mater. Sci.* 32, 400–406.
- Lazzeri, A., Bucknall, C., 1995. Applications of a dilatational yielding model to rubber-toughened polymers. *Polymer* 36, 2895–2902.
- Lemaitre, J., Chaboche, J.L., 1994. *Mechanics of Solid Materials*. Cambridge university press, Cambridge.
- Mathiesen, D., Vogtmann, D., Dupaix, R.B., 2014. Characterization and constitutive modeling of stress-relaxation behavior of poly (methyl methacrylate)(PMMA) across the glass transition temperature. *Mech. Mater.* 71, 74–84.
- Maurel-Pantel, A., Baquet, E., Bikard, J., Bouvard, J.L., Billon, N., 2015. A thermo-mechanical large deformation constitutive model for polymers based on material network description: application to a semi-crystalline polyamide 66. *Int. J. Plast.* 67, 102–126.
- Mulliken, A., Boyce, M., 2006. Mechanics of the rate-dependent elastic–plastic deformation of glassy polymers from low to high strain rates. *Int. J. Solids Struct.* 43, 1331–1356.
- Mullins, L., 1948. Effect of stretching on the properties of rubber. *Rubber Chem. Technol.* 21, 281–300.
- Nahshon, K., Hutchinson, J., 2008. Modification of the Gurson model for shear failure. *Eur. J. Mech. A Solid.* 27, 1–17.
- Nguyen, V.D., Lani, F., Pardoan, T., Morelle, X.P., Noels, L., 2016. A large strain hyperelastic viscoelastic-viscoplastic-damage constitutive model based on a multi-mechanism non-local damage continuum for amorphous glassy polymers. *Int. J. Solids Struct.* 96, 192–216.
- Nielsen, L.E., 1969. Cross-linking–effect on physical properties of polymers. *J. Macromol. Sci. Polymer Rev.* 3, 69–103.
- Ovalle Rodas, C., Zairi, F., Nait-Abdelaziz, M., 2014. A finite strain thermo-viscoelastic constitutive model to describe the self-heating in elastomeric materials during low-cycle fatigue. *J. Mech. Phys. Solids* 64, 396–410.
- Polanco-Loria, M., Clausen, A.H., Berstad, T., Hopperstad, O.S., 2010. Constitutive model for thermoplastics with structural applications. *Int. J. Impact Eng.* 37, 1207–1219.
- Polanco-Loria, M., Daiyan, H., Grytten, F., 2012. Material parameters identification: an inverse modeling methodology applicable for thermoplastic materials. *Polym. Eng. Sci.* 52, 438–448.
- Qi, H.J., Boyce, M.C., 2004. Constitutive model for stretch-induced softening of the stress–stretch behavior of elastomeric materials. *J. Mech. Phys. Solids* 52, 2187–2205.
- Qi, H.J., Boyce, M.C., 2005. Stress–strain behavior of thermoplastic polyurethanes. *Mech. Mater.* 37, 817–839.
- Ramakrishna, S., Mayer, J., Wintermantel, E., Leong, K.W., 2001. Biomedical applications of polymer-composite materials: a review. *Compos. Sci. Technol.* 61, 1189–1224.
- Shen, F., Hu, W., Meng, Q., 2015. A damage mechanics approach to fretting fatigue life prediction with consideration of elastic–plastic damage model and wear. *Tribol. Int.* 82, 176–190.
- Shen, F., Zhao, B., Li, L., Chua, C.K., Zhou, K., 2017. Fatigue damage evolution and lifetime prediction of welded joints with the consideration of residual stresses and porosity. *Int. J. Fatigue* 103, 272–279.
- Shen, F., Yuan, S.Q., Chua, C.K., Zhou, K., 2018. Development of process efficiency maps for selective laser sintering of polymeric composite powders: modeling and experimental testing. *J. Mater. Process. Technol.* 254, 52–59.
- Srivastava, V., Chester, S.A., Ames, N.M., Anand, L., 2010. A thermo-mechanically-coupled large-deformation theory for amorphous polymers in a temperature range which spans their glass transition. *Int. J. Plast.* 26, 1138–1182.
- Torres, J.P., Frontini, P.M., Machado, M., Major, Z., 2016. Deformation and failure of semicrystalline polymers under dynamic tensile and biaxial impact loading. *Int. J. Impact Eng.* 98, 52–61.
- Tvergaard, V., 1982. On localization in ductile materials containing spherical voids. *Int. J. Fract.* 18, 237–252.
- Voyiadjis, G.Z., Dorgan, R.J., 2007. Framework using functional forms of hardening internal state variables in modeling elasto-plastic-damage behavior. *Int. J. Plast.* 23, 1826–1859.
- Walvekar, A.A., Leonard, B.D., Sadeghi, F., Jalalhmadi, B., Bolander, N., 2014. An experimental study and fatigue damage model for fretting fatigue. *Tribol. Int.* 79, 183–196.
- Xiao, R., Sun, H., Chen, W., 2017. A finite deformation fractional viscoplastic model for the glass transition behavior of amorphous polymers. *Int. J. Non-Linear Mech.* 93, 7–14.
- Yu, C., Kang, G., Chen, K., 2017a. A hygro-thermo-mechanical coupled cyclic constitutive model for polymers with considering glass transition. *Int. J. Plast.* 89, 29–65.

- Yu, C., Kang, G., Chen, K., Lu, F., 2017b. A thermo-mechanically coupled nonlinear viscoelastic–viscoplastic cyclic constitutive model for polymeric materials. *Mech. Mater.* 105, 1–15.
- Zaïri, F., Nait-Abdelaziz, M., Woznica, K., Gloaguen, J.-M., 2005. Constitutive equations for the viscoplastic-damage behaviour of a rubber-modified polymer. *Eur. J. Mech. A Solid.* 24, 169–182.
- Zaïri, F., Nait-Abdelaziz, M., Gloaguen, J.M., Lefebvre, J.M., 2011. A physically-based constitutive model for anisotropic damage in rubber-toughened glassy polymers during finite deformation. *Int. J. Plast.* 27, 25–51.
- Zerbe, P., Schneider, B., Moosbrugger, E., Kaliske, M., 2017. A viscoelastic-viscoplastic-damage model for creep and recovery of a semicrystalline thermoplastic. *Int. J. Solids Struct.* 110–111, 340–350.